Sea Surface Temperature Contrast in Tropical World: Part 1 Mean State

Dennis L. Hartmann[1], Brittany D. Dygert[1], Qiang Fu[1]and Peter N. Blossey[1]

[1]Department of Atmospheric Sciences, University of Washington, Seattle, Washington 98195

Key Points:

- The SST contrast increases with warming, because the clear-sky greenhouse effect feedback on SST contrast is stronger than the offsetting cloud feedback
- As the climate warms, the cooling rate of the atmosphere increases by moving upward and increasing in strength, giving a more top-heavy cooling profile
- The stronger and more top-heavy cooling rate profile supports stronger mass circulation and increased cloud ice as the climate warms

Corresponding author: Dennis L. Hartmann, dhartm@uw.edu

Abstract

Warming experiments with a uniformly insolated, non-rotating climate model with a slab ocean are conducted by increasing the solar irradiance. As the climate warms, the surface temperature contrast between the warm, rising and cooler, subsiding regions increases, mostly driven by the stronger greenhouse effect in the warm region. Cloud changes act to decrease the surface temperature contrast. The clouds in the convective region become much more reflective as the climate warms, acting to reduce the surface temperature contrast. It is argued that the increase in cloud ice in the convective region is associated with stronger clear-sky radiative cooling in the upper troposphere in warmer climates. This more top-heavy radiative cooling rate can be explained with simple theory. The mass circulation rate between warm and cool regions consists of shallow and deep cells. Both cells increase in strength with warming. The lower cell remains connected to the surface, while the upper cell rises to maintain a roughly constant temperature. At temperatures above about 310K surface temperature contrast begins to decline, and the climate becomes more sensitive. The reduction in SST contrast above 310K again appears to be initiated by clear-sky radiative processes, although cloud processes in both the rising and subsiding regions contribute. The response of clear-sky outgoing longwave to surface warming begins to accelerate in the region of rising motion and decline in the region of subsidence, resulting in a smaller SST contrast.

Plain Language Summary

A global model of a non-rotating Earth with an ocean that stores heat but does not transport it is run to equilibrium with different values of globally uniform solar heating. Despite the complete uniformity of the system, it develops regions of warm sea surface temperature where rain and rising motion occur, and regions with downward, subsiding air motion where rainfall does not occur. These contrasts between rainy and dry regions look very similar to what is observed in the present-day tropics. As the climate is changed from current temperatures toward warmer temperatures, the warm regions warm faster, mostly because the rising regions contain more water vapor. The clouds rise to higher altitudes in the warmer climates, and produce more cloud ice. These changes are shown to arise from well-understood physical processes that are expected to operate in nature.

1 Introduction

Sea surface temperature (SST) contrast within the tropics has received increasing interest because of its apparent role in the pattern effect on climate sensitivity (Zhou et al., 2016; Andrews et al., 2018) and because the maximum tropical SST plays such an important role in setting the state of the tropical atmosphere, which has near global effects (Dong et al., 2019). The interaction of the atmosphere with the tropical ocean currents can have a large impact on the SST structure within the tropics. Weakening of the strength of tropical overturning with warming can project strongly onto the east-west Walker Circulation in the tropical Pacific ocean, leading to variations in the strength of upwelling in the equatorial Pacific (Knutson & Manabe, 1995; Vecchi & Soden, 2007). A weakening of the Walker Circulation with warming might lead to a reduction in the SST contrast, but other arguments suggest that SST contrast associated with tropical upwelling should increase in a warming Earth (Clement et al., 1996; Kohyama et al., 2017; Seager et al., 2019).

In this study we will use a slab ocean model and thus dispense with effects related to ocean heat transports to focus on basic thermodynamic mechanisms for controlling tropic SST contrast. These mechanisms include the differential greenhouse effect between moist and dry regions, the cloud feedbacks in the rising and subsiding regions, and the movement of energy between the warm and cool regions by atmospheric transport. These

mechanisms have been studied individually previously, but generally not within the context of a global climate model. The enhanced greenhouse effect in moist regions of the tropics was studied in observations and radiative transfer modeling by Inamdar & Ramanathan (1994). Pierrehumbert (1995) used a two-box modeling framework to show the importance of dry regions of the tropics for stabilizing the greenhouse effect feedback within the tropics. Ramanathan & Collins (1991) used observations to show that tropical ice clouds associated with convection shade the warm regions of the tropics and proposed that this would provide an upper limit on tropical SST. Miller (1997) showed in a box model that increasing lower tropospheric stability in a warmed tropics could increase low clouds and thereby reduce the sensitivity of climate. Enhanced low cloud in the subsiding region would increase the SST contrast, all else being equal. Bony et al. (2016) argue that deep convective cloud fraction declines with SST due to increasing stability with decreasing pressure at cloud top, while Held & Soden (2006) argue that basic thermodynamic constraints require the convective mass flux to decline in a warming climate. The average cloud top temperature in the convective region is predicted to remain roughly constant during cliamte change (Hartmann & Larson, 2002).

To study the interactions among the thermodynamic mechanisms described above requires a model that can produce a state-of-the-art simulation of the interaction between large-scale circulation and the radiative processes associated with low boundary layer clouds in the subsiding region and deep convective clouds in the region of rising motion. Convection-permitting models with horizontal resolution of the order of 1km can operate without the use of a convection parameterization, but this resolution may not be sufficient to simulate the eddies that are critical for boundary layer clouds or anvil ice clouds. These models are generally not tuned to current observations, as global climate models are, and they are not converged, in the sense that they produce a range of behaviors on key metrics that are as wide or wider than that of global climate models (Wing et al., 2020). Finally, to simulate the interaction of convection with large-scale circulation in a convection-permitting model requires a substantial investment in computational resources. For these reasons we believe it is useful to investigate these interactions with a global climate model with horizontal resolution of the order of 100km, since these models have been validated against observations and are much more computationally efficient, even though some of the critical physical processes are represented with imperfect parameterizations. To focus more specifically on the processes operating within the tropics, we make the insolation uniform and set the rotation to zero. The simulations are thus a radiative convective equilibrium (RCE) calculation, in a model in which SST can respond at large scale.

The tropical atmosphere exhibits regions of consistently active deep convection, where the SST is generally higher and the free troposphere is more humid, and regions where deep convection is rare, the air is dry, and the SST is slightly lower. The tropical ocean has large regions where the SST is high and relatively uniform, especially in the western Pacific and Indian Ocean regions. Much of the deep tropical convection occurs in this 'warm pool' region. The horizontal energy exchanges between the warm pool and other regions of the tropics are generally small ($\sim$ 35 Wm^{-2}) compared to the vertical exchanges of energy between the surface, the atmosphere and space ($\sim$ 300 Wm^{-2}), so radiative-convective equilibrium (RCE) is a useful approximate model of the tropical and even the global climate (Manabe & Wetherald, 1967).

RCE has been studied with one-dimensional models, with limited-domain cloud-resolving models and with global general circulation models (GCM). High-resolution models in a limited domain can be a means of studying the detailed physics of tropical convection and have revealed the tendency of convection to aggregate within a sufficiently large model domain (Bretherton et al., 2005; Cronin & Wing, 2017; Held et al., 1993; Tompkins, 2001a). RCE simulations have also been done with models in which the convection is parameterized (Held et al., 2007; Larson & Hartmann, 2003b,a). Investigat-

ing RCE in climate models with parameterized convection is done with several goals in mind (e.g. Wing et al. (2018)). One goal is to better understand how the parameterizations within the models perform in such simulations. In addition, more fundamental understanding of how the climate system works might be gained if it can be shown that the behaviors of interest result from fundamental physical constraints that are not too dependent on the details of the parameterizations used in the models. It is this second goal that we pursue in this study.

Simulations of RCE with global climate models (GCM) can be performed with fixed sea surface temperatures (SST) (Coppin & Bony, 2015; Held et al., 2007; Retsch et al., 2019) or with a slab ocean, for which the SST interacts with atmospheric processes (Popke et al., 2013; Reed et al., 2015). In these simulations the convection aggregates in a portion of the model domain, in a fashion similar to cloud-resolving models. The self-aggregation process seems to be associated with a preference for convection to be located in regions that have already been moistened by convection, where radiative and microphysical interactions will favor further convection (Bretherton et al., 2005; Tompkins, 2001b; Wing & Emanuel, 2014). Becker et al. (2017) have shown that convective aggregation in GCMs is sensitive to the convective parameterization. GCMs with fixed SST have also been used to show the importance of cloud radiative effects on large-scale circulation (Harrop & Hartmann, 2015, 2016; Albern et al., 2018).

In a model with an interactive slab ocean, the ocean tends to be warm under the enhanced water vapor and cool elsewhere. This convection-SST interaction results in the organization becoming stronger and taking larger spatial and temporal scales. One particular case of interest is a "Tropical-World" simulation in which the planet does not rotate and the insolation is globally uniform. When done with a slab ocean model, these simulations typically develop large-scale persistent regions where SST is high and convection is common, and regions where SST is lower and convection is unlikely, much like the observed tropics (Popke et al., 2013; Reed et al., 2015). These simulations typically also have a limit cycle in which the SST contrast and the degree of aggregation oscillate at periods that depend on the mean SST and the depth of the mixed layer (Coppin & Bony, 2017).

In this study we will consider Tropical-World (TW) simulations with the GFDL AM2.1 model with a slab ocean. We will focus primarily on the processes that determine the SST contrast in the equilibrated climate of the model. The mechanisms of the oscillation will be studied in a separate paper. In particular, we wish to better understand the mechanisms whereby the SST, atmospheric circulation, evaporation and clouds interactively self-regulate. We will argue that these mechanisms are relevant to the observed tropical climate. Understanding the mechanisms that control the SST contrast within the Tropics is particularly important because it has been shown that the apparent sensitivity of climate is affected by the SST contrast. Zhou et al. (2016) showed with observations and modeling that SST pattern changes may have led to low cloud changes that suppressed global warming during recent decades. Dong et al. (2019) have shown in a modeling study that the change in SST over the western tropical Pacific warm pool is a key determinate of the net cloud feedback globally.

In this study we will investigate the mechanisms that maintain the SST contrast in the equilibrated climate, and their sensitivity to warming. We find that as we warm the climate from one similar to the present-day tropics, the average SST contrast in the model increases, because the stronger greenhouse effect in the rising region overwhelms the cloud feedbacks, which act to reduce the SST difference. As the climate warms, the convective heating rate is shifted upward, becoming more top-heavy, consistent with the production of more ice in the convective regions. We will show that the enhanced cooling rate in the upper troposphere is a simple consequence of radiative-convective equilibrium and can be reproduced with a simple 1-D RCE model with fixed relative humidity and adjustment to a moist adiabatic lapse rate. We propose that radiatively-driven

ice increase is a useful complement to the idea that a warmer moister surface will result in more ice for a fixed precipitation efficiency (Zhao, 2014; Zhao et al., 2016). For mean SST values between 300 and 309K the global mean SST is fairly insensitive to forcing, primarily because of the efficient longwave cooling in the subsiding region and because the net cloud response does not change the albedo as the climate warms. As the SST exceeds 310K the climate becomes much more sensitive because the greenhouse effect feedback in the subsiding region becomes more strongly positive and the SST contrast declines. The shortwave cloud effect feedback acts to reduce the SST contrast at all SSTs tested, and this effect also becomes stronger above 310K and helps to reduce the SST contrast at these warmer temperatures. The mass overturning consists of a lower cell driven by radiative cooling in the lower troposphere of the subsiding region, and an upper cell driven by radiative cooling in the upper troposphere. The mass circulation in both these cells increases with global mean SST up to 309K, beyond which they decline with the decreasing SST contrast.

2 Model and Experimental Description

The model used is GFDL's CM2.1 Global Coupled Climate Model with a slab ocean model (Anderson et al., 2004; Delworth et al., 2006). The rotation rate is set to zero and the insolation is globally uniform. CO_2 is set to 324 ppm and CH_4 to 1650 ppb. Ozone is fixed to the observed tropical mean profile as a function of pressure. A horizontal spatial resolution of 2°latitude by 2.5°longitude, 32 vertical levels, and a time step of 900 seconds were used for the control experiments. The vertical spacing is less than 25hPa in the boundary layer, and is nearly identical to the 24-level CM2.1 vertical resolution used for CMIP5. An additional 8 levels have been added in the upper troposphere and stratosphere to better represent the extreme warming simulations included here. Experiments were also conducted with 64 vertical levels, and with 24 vertical levels and increased horizontal resolution. While increased resolution changes the mean SST, the basic conclusions about the responses to warming we reach here are not affected. The 64-level simulations produce the same dependence of mass circulation on mean SST as the 32-level simulations, and a similar transition to higher sensitivity and lower SST contrast around 310K, for example. It is very likely that some model behavior is sensitive to the details of the cloud and convection parameterizations, so our conclusions should be tested with other climate models and cloud-resolving models, but that is beyond the scope of the present work.

A set of seven basic experiments were completed using a 50-meter slab ocean depth and incoming solar irradiance corresponding to the annual and diurnal averages at latitudes of 26°, 28°, 30°, 33°, 36°, 38°, and 45°: giving four hot climates, two climates corresponding to the current Tropics and a climate with the surface temperature of the current global average (Table 1). Each experiment was run long enough to produce 40 years of stable climate for analysis after an initial spin up period that depends on the mixed-layer depth and starting climate. These experiments are denoted by their approximate global mean SST. For example, the control experiment with an insolation of 342 Wm^2 and SST of 301.2K is called "C301". If the slab ocean is reduced to 12-meter depth the model has more high frequency variability, but the basic features emphasized here are present. We have also done some experiments to test how the model behavior is different if it is forced with CO_2 increases rather than insolation increases. Some modest differences appear, but the equilibrated climates discussed here are mostly controlled by hydrologic feedbacks that depend more on the mean temperature change than on the means by which that temperature change is forced (see Supplementary Material).

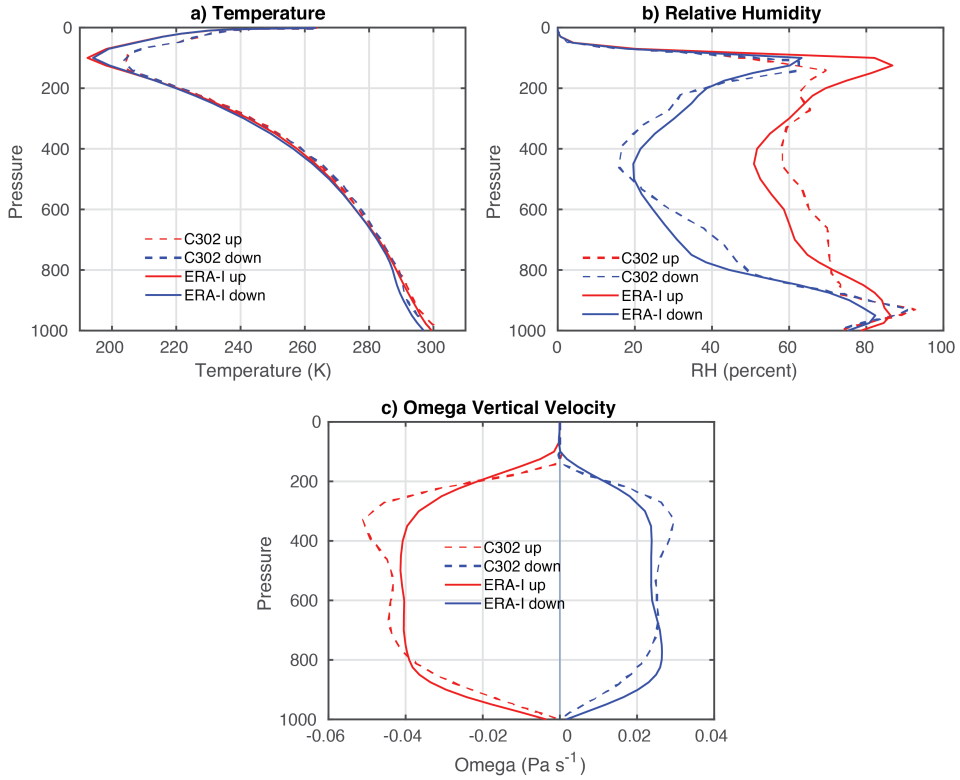

Figure 1. Comparison of a) Temperature, b) Relative humidity and c) vertical motion profiles versus pressure (hPa) in regions of upward and downward motion for the average of monthly mean fields from ERA-Interim Reanalysis in the region within 22.5S to 22.5N and 90E to 270E, and the global average of monthly means for the C302 experiment, which has a global mean SST closest to the observed tropics.

3 Comparison to Observed Tropics

In this section we explore how accurately TW emulates the observed Tropics for cases with similar SST to the current tropics, *e.g.* C302. Despite their simplifications, TW simulations have some basic characteristics in common with the observed tropics, so that we can argue they are a plausible analog to the observed tropics for our purposes. In particular, the vertical structure of temperature, relative humidity and mean vertical motion are important for what we want to investigate, and those very closely resemble the observed tropics.

To compare the model output to observations we use monthly SST data from NOAA OI interpolated data (Reynolds et al., 2007), radiation budget observations from CERES EBAF version 4 (Loeb et al., 2018). Atmospheric data and surface turbulent fluxes are from the ERA-Interim product (Dee et al., 2011). The period of overlap used is from March 2000 until October of 2018. Figure 1a shows that the temperature profile in the TW simulation is similar to that in the real tropics. The inversion in the subsiding region is stronger and closer to the surface in the model compared to observations, but the air temperature contrast in the boundary layer is smaller. The tropopause is warmer in the model, probably because the model does not have a Brewer-Dobson circulation in the stratosphere (Birner, 2010). The relative humidity in both the model and the observations is determined by transitioning linearly from relative humidity above water to relative humidity above ice in the temperature range from 0 to -20°C. The relative humidity dis-

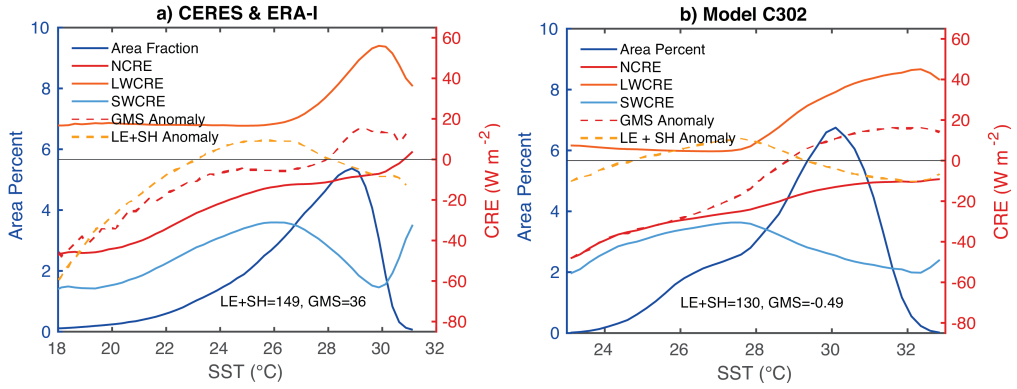

Figure 2. Area fraction occupied by SST values, Cloud Radiative Effects (CRE), heating of the atmosphere by turbulent fluxes of latent and sensible heat at the surface (LE+SH), and vertically integrated export of energy by atmospheric motions (GMS). Turbulent fluxes and atmospheric export are plotted as anomalies from the area average over all SST values. a) CRE from CERES and energy fluxes ERA-Interim reanalysis for the region from the ocean regions between 22S-22N, b) the same quantities from the model run C302, which has a mean SST close to the observed Tropics of Earth.

tribution is similar to observations in the upward and downward regions to within 10%, but the model has a more uniform distribution of relative humidity in the region of rising motion, with larger humidity in the middle troposphere and lower humidity under the cold point in the region of rising motion. The lower humidity at the tropopause in the model may again have to do with the absence of a Brewer-Dobson Circulation. The vertical velocity structures in the upward and downward regions also agree with observations. The vertical velocity increases rapidly away from the surface, stays relatively constant and then decreases rapidly above 300hPa. Later we will show that this structure is associated with a two-cell structure of the mass circulation. The shallow cell is associated with the lower boundary and the deeper cell is associated with the radiative cooling of the upper troposphere.

Figure 2 shows that the model has a similar negatively-skewed SST distribution as the real tropics, although the negative tail is not as long, likely because of upwelling regions within the tropical oceans. The longwave and shortwave cloud radiative effects (LWCRE and SWCRE) increase toward the warmest SST, but their sum, the net cloud radiative effect (NCRE) is much weaker and does not vary much within the warm pool. Over the warmest water the net cloud radiative effect is small, negative and almost independent of SST, although more negative than in the observations. The cloud radiative effects do not become smaller at the highest SST values as in the observations. This is likely because in observations the highest SST regions tend to occur where cloud and precipitation are consistently suppressed by large-scale circulations associated with fixed geographical features such as land and sea distributions (Waliser & Graham, 1993). Those fixed constraints do not exist in TW, where high SST regions quickly attract convection and clouds, which cool the surface and suppress the positive tail of the SST distribution.

Also shown on Figure 2 are the cooling of the surface by turbulent fluxes (LE+SH) and the net export of energy in the atmosphere (GMS). The turbulent cooling of the surface declines toward the maximum SST values, while the atmospheric energy export peaks at the warmest temperatures. The observed tropical atmosphere exports about 35 Wm^{-2} to the extratropics but the net atmospheric export of energy in TW is zero. The mean

export of energy (GMS) from the warmest regions in TW is about 20 Wm^{-2} and declines as the climate is warmed (Table 1).

Case	Insol	SST	T_{dif}	Precp	SF	RH	OLR	Albedo	RHR	GMS	T_{up}-T_{dn}
C289	307.2	288.7	6.1	2.8	0.58	48.9	234.7	0.24	-0.76	18.2	1.5
C302	342.4	302.1	7.0	4.2	0.63	47.0	266.7	0.22	-1.02	24.0	1.7
C303	349.3	303.5	8.0	4.5	0.65	46.0	271.5	0.22	-1.10	22.6	2.5
C307	364.4	306.8	9.7	5.1	0.67	44.6	284.7	0.22	-1.28	14.0	3.7
C309	376.3	309.2	11.1	5.6	0.67	43.6	295.1	0.22	-1.42	11.0	4.6
C313	383.6	312.9	8.9	6.1	0.68	43.1	306.0	0.21	-1.55	10.0	3.3
C318	390.5	318.4	6.3	6.4	0.75	42.8	317.3	0.19	-1.70	-1.1	1.6

Table 1. Insolation is in Wm^{-2}, Temperatures are in Kelvin, Precipitation is in mm day^{-1}, SF is subsiding fraction, RH is relative humidity in percent averaged over mass, RHR is radiative heating rate in $Kday^{-1}$, averaged over mass, GMS is the atmospheric transport from the region of upward motion in Wm^{-2}.

4 Mean Properties versus SST

In this section we describe the response of various global mean properties to global mean SST. Table 1 shows some climatological mean values for the seven control cases. The global albedo remains constant at about 22% for global mean SST between 302K and 309K, then declines for warmer SST values. Relative humidity declines slowly with warming, while subsiding fraction increases. Subsiding fraction is determined from the monthly and mass-averaged pressure velocity.

Figure 3a shows Tdif, the SST contrast for the top 20% of SST values minus the bottom 20% of SST values, as well as the difference between the SST in regions where the mass-averaged velocity is upward and downward. These differences increase for mean SST values between 302K and 309K, and then decline for larger mean SST values. The difference in net radiation also increases and then declines (Fig. 3b). Fig. 3c shows that the sensitivity of the global mean SST to insolation is small in the SST range of 302-309K, but then increases for warmer SSTs. An increase in climate sensitivity at temperatures around 310K has previously been reported for other models and attributed primarily to water vapor feedback (Meraner et al., 2013; Russell et al., 2013).

The model sensitivity can be calculated from the values in Table 1 by taking the ratio of the mean SST change to the forcing for the C309 and C302 cases. Since the albedo remains constant at 22%, we can compute the forcing as the change in insolation multiplied by 0.78, the fraction of that change in insolation that is absorbed, giving a forcing of $26.45\mathrm{Wm}^{-2}$. The global mean SST change is 7.1K, so that the sensitivity parameter is $7.1\mathrm{K}/(26.45\mathrm{Wm}^{-2}) = 0.27\ \mathrm{K}/(\mathrm{Wm}^{-2})$, which means it would take almost $4\mathrm{Wm}^{-2}$ of forcing to warm the SST by 1K. The primary reason for the low sensitivity of the model is the strong sensitivity of the OLR to surface temperature, 4 $Wm^{-2}K^{-1}$ between 302K and 309K. Consistently with the more efficient atmospheric longwave cooling, the hydrological sensitivity of $4\%K^{-1}$ is also large compared to typical global models (Pendergrass & Hartmann, 2014).

A key to understanding the insensitivity of the model is then to consider the longwave greenhouse effect (GHE) changes. The GHE is defined here to be the difference between the longwave emission from the surface and the outgoing longwave radiation (OLR)

(Inamdar & Ramanathan, 1994).

$$GHE = \sigma T_s^4 - OLR \tag{1}$$

Here σ is the Stefan-Boltzmann constant and T_s is the surface temperature. Figure 3d shows the GHE in the upward and downward regions for clear and average conditions. Between mean SSTs of 302K and 309K the greenhouse effect in the subsiding region remains roughly constant, meaning that the OLR increases at about the same rate as the surface emission. This is a reflection of the stabilizing effect of the dry 'radiator fins' as described by Pierrehumbert (1995). The subsiding region atmospheric temperatures increase at the same rate as the rising region temperatures, but the relative humidity is lower, so that the emission to space increases rapidly with mean surface temperature.

The greenhouse effect is also the primary driver of the growth in SST contrast with warming. The greenhouse effect grows by $50\mathrm{Wm}^{-2}$ in the upward region, but hardly at all in the downward region. Inamdar & Ramanathan (1994) showed how relative humidity in the warm, moist regions of the tropics can cause a super greenhouse effect in those regions. Figure 3d shows that in the upward region LWCRE stays almost constant as the climate is warmed. The difference between the clear-sky emission temperature and the cloud top temperature remains constant, because both are tied to air temperature through the Clausius-Clapeyron dependence of saturation vapor pressure on temperature (Hartmann et al., 2019). Thus cloud longwave effects do not play a central role in the increase in SST contrast with warming, which is mostly a clear-sky radiative effect. The stabilization of climate by enhanced emission to space from the subsiding regions is enhanced when the SST contrast increases with warming. Increasing SST contrast causes the mean atmospheric temperature to increase faster than the mean surface temperature, causing a substantial negative feedback.

To understand how the greenhouse effect changes with mean temperature it is helpful to decompose the OLR into contributions from net surface loss and atmospheric cooling. Start with the equation for the longwave cooling rate of the atmosphere as a function of the net longwave flux in the upward direction, F, where c_p is specific heat at constant pressure, ρ_{Air} is air density and z is altitude.

$$\left.\frac{dT}{dt}\right|_{LW} = -\frac{1}{\rho_{Air}\, c_p}\frac{dF}{dz} \tag{2}$$

Integrating this equation though the mass of the atmosphere after using the hydrostatic relationship we obtain.

$$OLR = F(p_s) \; - \int_0^{p_s} c_p \left.\frac{dT}{dt}\right|_{LW} \frac{dp}{g} \tag{3}$$

$$= \quad F_0 \quad + \quad F_A \tag{4}$$

The OLR thus consists of two terms; the net longwave flux upward at the surface (F_0), plus the mass integral of the longwave radiative cooling rate (F_A). Figure 4a shows the OLR and the contribution to the OLR from the atmospheric cooling rate, F_A , for the upward and downward regions. The difference between OLR and F_A is the surface contribution F_0. In the region of rising motion, because the relative humidity is so high and clouds are present, the OLR does not increase very much in the range of temperatures between 300 and 310K. This is mostly because the net longwave loss at the surface is declining, primarily as a result of increased water vapor continuum absorption in the window region (e.g. Hartmann (2016), Fig. 10.10 and Koll & Cronin (2018)). The atmospheric cooling rate increases almost linearly with temperature across the entire range of SST values for reasons that we will explore subsequently by looking at the cooling rate as a function of pressure.

Figure 4a shows that in the region of subsiding motion the cooling rate of the atmosphere, F_A , increases more rapidly than in the region of upward motion, again prin-

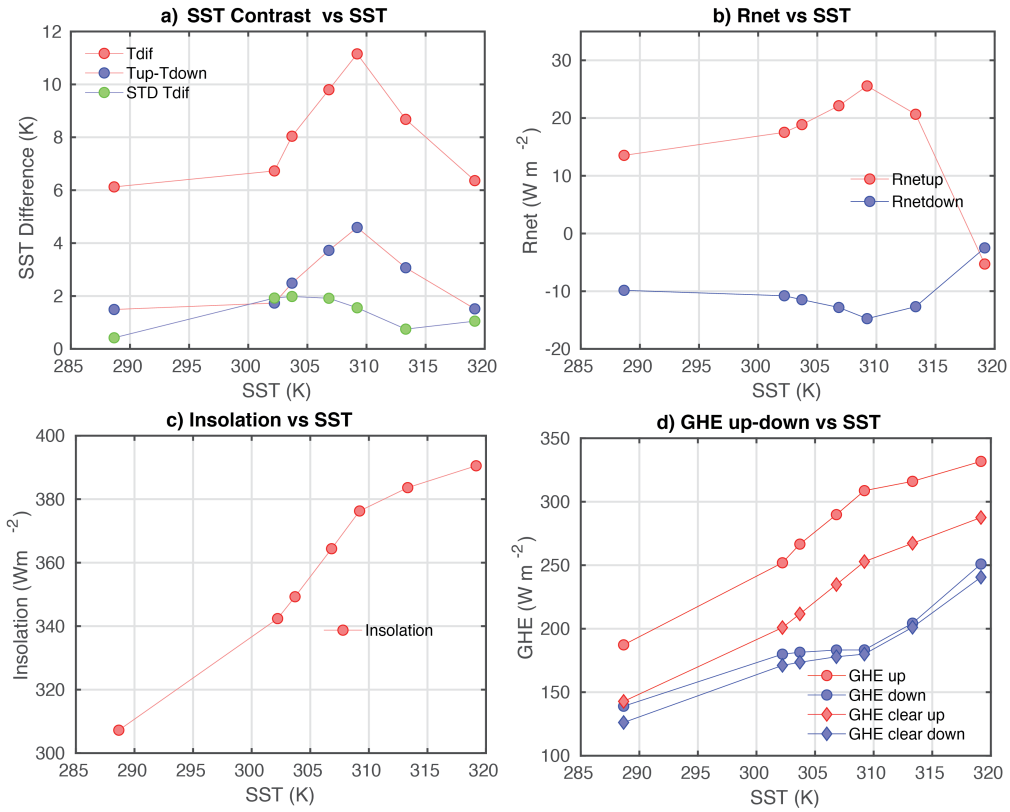

Figure 3. a) SST contrast as a function of mean SST, Tdif is the difference between the warmest and coldest 20% of SST values, Tup-Tdown is the SST difference between regions of upward and downward motion. The standard deviation with time of the monthly mean SST is also shown. b) the net radiation at the top of the atmosphere in the upward and downward regions, c) the insolation used in the experiment as a function of the global mean SST in equilibrium, d) the greenhouse effect in the upward and downward regions for both average and clear-sky conditions.

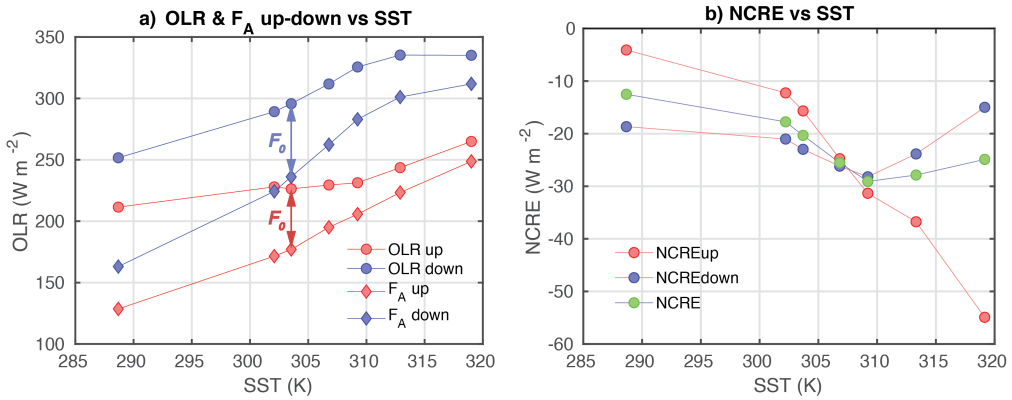

Figure 4. a) OLR and atmospheric cooling rate contribution to OLR from F_A and F_0 in the upward and downward regions as a function of global mean SST for the seven basic experiments. F_0 is the difference between OLR and F_A, as indicated by the arrows for case C303. b) Net Cloud Radiative Effect (NCRE) for upward, downward and global mean averages

cipally because of the relative humidity distribution, but also because the air temperature is linked very closely to that in the region of rising motion, where it follows a moist adiabat tied to the near surface temperature. The net surface radiation loss decreases with increasing SST, but the emission from the atmosphere increases sufficiently fast to overcome this effect so that OLR increases at the same rate as the surface emission, as shown in Figure 3d. The insensitivity of the clear-sky greenhouse effect in the subsiding region to mean warming depends strongly on Tdif, the SST contrast parameter, since the atmospheric emission temperature in the subsiding region is tied to the warmer SST in the rising region. Motions quickly respond to redistribute mass to decrease pressure gradients. This dynamic balance also explains why the air temperature above the boundary layer in the subsiding region is slightly warmer than the air temperature in the rising region, when the air temperature below the inversion is colder in the subsiding region (Fig. 1a). Above mean SST of 310K, the surface longwave loss, F_0, reaches a limiting value and the OLR must follow the linearly increasing F_A. This increases the local climate stability in the warm region. In the subsiding region the OLR stops increasing above 310K because the surface longwave loss declines, but also because the atmospheric cooling rate begins increasing much more slowly with increasing SST.

Cloud radiative effects are also important. Fig. 4b shows that net cloud radiative effect (NCRE) in the region of upward motion becomes more negative by about $20\mathrm{Wm}^{-2}$ between 302 and 309K, while Fig. 3d shows that the GHE becomes more positive by about $50\mathrm{Wm}^{-2}$. We thus conclude that the increased cloud shading is acting to suppress the warming in the upward region, but it is overwhelmed by the increases in the clear-sky GHE there, causing the SST to warm more rapidly in the upward region. Beyond 309K the SWCRE in the upward region continues to become more negative. The NCRE in the subsiding region does not change as much as in the rising region. Because the insolation is being increased to warm the model, it is instructive to normalize the SWCRE by the insolation, so that it forms the negative of the albedo enhancement by clouds (not shown). The normalized SWCRE in the subsiding region becomes slightly more positive as the climate is warmed, especially for SSTs greater than 309K. In contrast, the normalized SWCRE in the upward region becomes more negative with SST and by a larger amount. The SWCRE changes are thus working to reduce the SST contrast, while the greenhouse effect is responsible for the increase in SST contrast.

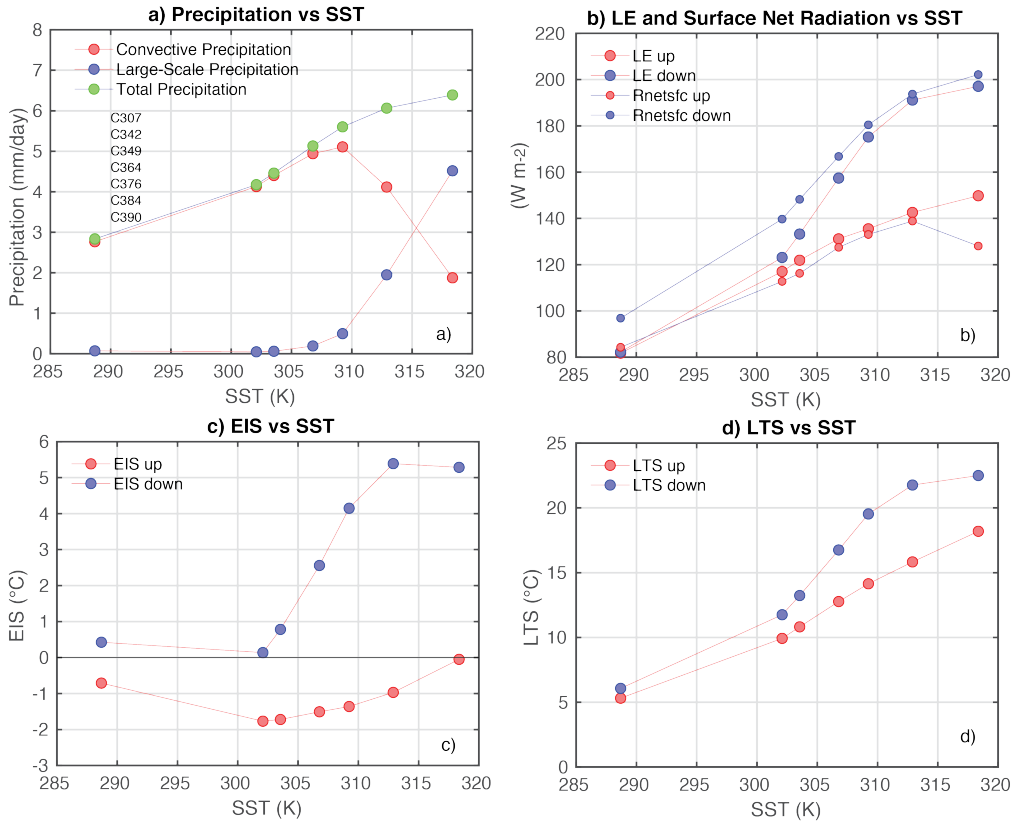

Figure 5. a) Precipitation, b) Surface evaporative cooling rate (LE) and Surface net radiative flux, c) Estimated inversion strength (EIS) and d) Lower Tropospheric Stability (LTS) as functions of SST for the seven control experiments.

Figure 5a shows the convective, large-scale and total precipitation rates as a function of SST for the control experiments. Above 310K the large-scale parameterization produces increasing fractions of the total precipitation. Held et al. (2007) noted that the AM2 model has a tendency to produce more precipitation from the large-scale parameterization in warm climates. In the next section we will argue that the increasing contribution of the large-scale parameterization to precipitation is a response to the radiative cooling rate becoming more top-heavy with warming. Figure 5b shows that the evaporative cooling rate closely follows the net radiative heating of the surface, since the sensible cooling and heat storage are both small. This suggests that evaporation and solar absorption are closely linked. The inversion strength, whether measured by Estimated Inversion Strength (EIS, Wood & Bretherton (2006)) or Lower Tropospheric Stability (LTS, Klein & Hartmann (1993)) increases particularly strongly across the range of temperatures from 300 to 310K (Figures 5c,d). In section 6.4 we will show that despite the increasing lower tropospheric stability, the low clouds in the subsiding region do not show a proportionate increase in area coverage or water content.

5 Properties in SST-Area Coordinates

As suggested by Figure 2, SST is a useful coordinate with which to organize an analysis of these simulations. We divide the SST into 0.25K intervals and then compute the area-averaged atmospheric structure for those SST bins. Each monthly grid cell from 40 years of simulation is identified by its SST, and variables of interest such as vertical velocity, relative humidity, etc, are averaged into the SST bin, where the area of the grid cell is taken into account to produce an SST composite. Each SST bin also has a value that determines what fraction of the total area of the globe falls within the SST bin, $f_A(SST)$, which was shown in Figure 2b for case C302. The cumulative area fraction is computed by integrating this pdf of area fraction across SST.

$$F_A(SST) = \int_0^{SST} f_A(SST)\, dSST \tag{5}$$

A streamfunction can be computed by integrating the omega vertical velocity in Pa/s through area,

$$\Psi(F_A, p) = \frac{A_E}{g} \int_0^{F_A} \omega(p)\, dF'_A \tag{6}$$

Here A_E is the surface area of Earth, g is the acceleration of gravity and $\Psi(F_A, p)$ has units of kg/s. The horizontal area velocity in $m^2 s^{-1}$ flowing toward the region of warm SST is then computed from,

$$V = -g\, \frac{d\Psi}{dp} \tag{7}$$

and the pressure velocity can be obtained from

$$\omega = \frac{g}{A_E}\, \frac{d\Psi}{dF_A} \tag{8}$$

We can then plot vertical profiles of atmospheric variables in the same coordinate system of area fraction ordered by SST (Figure 6). The air temperature varies from cold to warmer near the surface, as expected from the SST values, but in the middle and upper troposphere the air temperature does not vary much with SST. This is because, without rotation, gravity waves quickly adjust the atmospheric temperature to be nearly equal everywhere, except over the cold region where an inversion is present and some vertical compensation by warmer air aloft is necessary to keep the surface pressure gradients small.

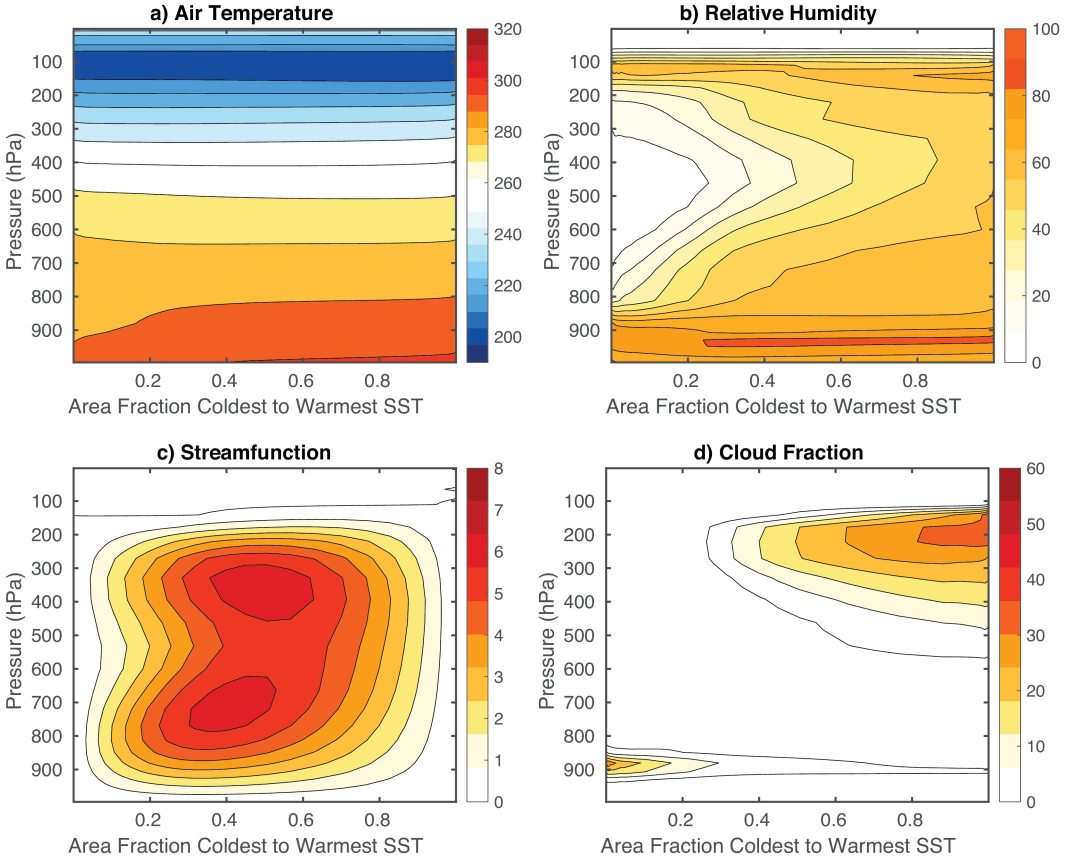

Figure 6. a) Air temperature (c.i. 10K), b) Relative humidity (c.i. 10%), c) Streamfunction (c.i. $1.0x10^{11} kg\ s^{-1}$) and d) Cloud Fraction (c.i. 10%) as functions of air pressure in hPa, plotted as functions of cumulative area fraction, F_A from coldest to warmest SST for case C302.

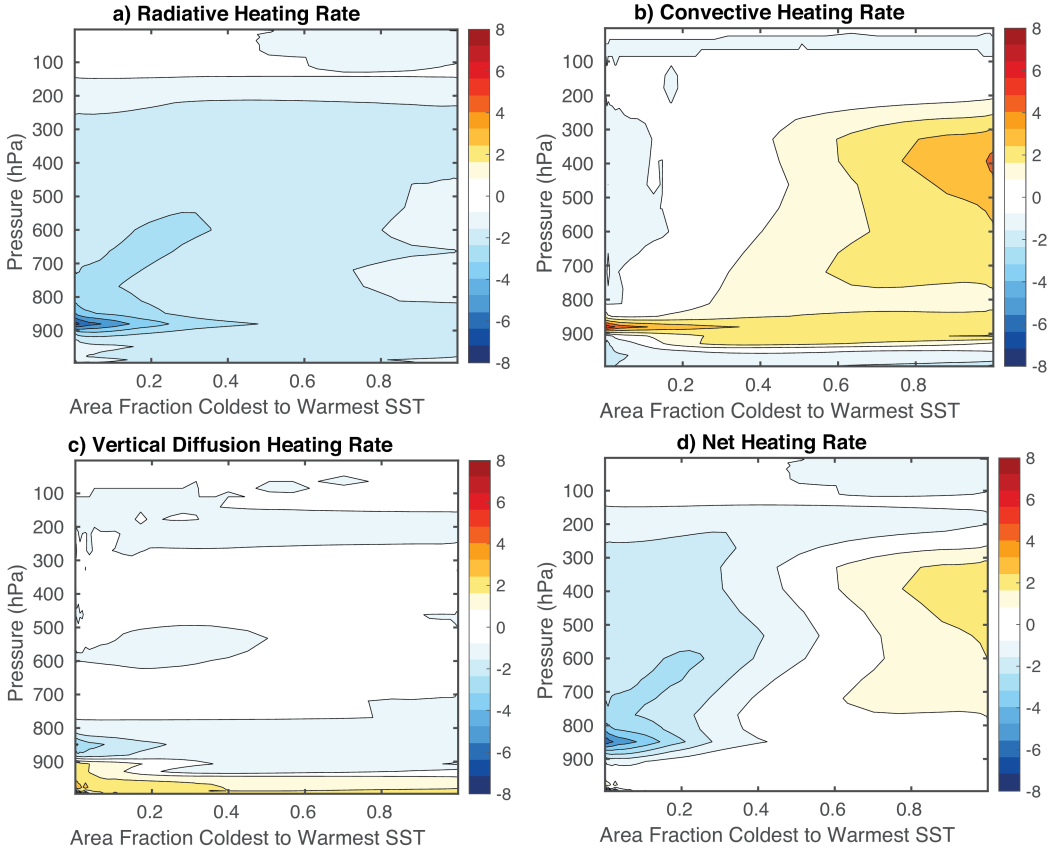

Figure 7. As in Figure 6 except a) Radiative Cooling Rate, b) Total Convective heating rate, c) Heating by Vertical Diffusion and d) Total net diabatic heating. (c.i. 1.0 $Kday^{-1}$).

The relative humidity (6b), on the other hand shows a great deal of variation across SST from less than 10% in the middle troposphere above the cooler SST to much higher values over warmer SST and near the surface and tropopause. The relative humidity is related to the vertical velocity, which is upward over the warmer SST and downward over the cooler SST (6c). Note that the strength of the mass circulation is about an order of magnitude bigger than the zonal Hadley Cell, since the Hadley Cell only incorporates the meridional mass circulation and is constrained to the tropics. This circulation has two distinct maxima, however, one in the lower troposphere and one in the upper, with two corresponding maxima in vertical velocity over the cooler water. It is this double-cell forcing that gives the observed vertical velocity its almost square structure seen in Figure 1. Cloudiness shows large coverage by high ice clouds above the warmer SST, and boundary layer clouds in the region of coolest SST (Figure 6d).

The streamfunction can be better understood by considering the diabatic heating processes that drive it. Figure 7 shows the diabatic heating values associated with radiation, convection and vertical diffusion. The shallow circulation cell is driven by radiative cooling associated with the low cloud tops and the relative humidity gradient at and above the boundary layer top in the subsiding region. The radiative cooling associated with the relative humidity gradient in the lower troposphere of the subsiding region serves to deepen the shallow circulation beyond what it would be from boundary layer processes alone. The deep circulation cell is driven by the deep radiative cooling and the compensating convective heating in the rising region.

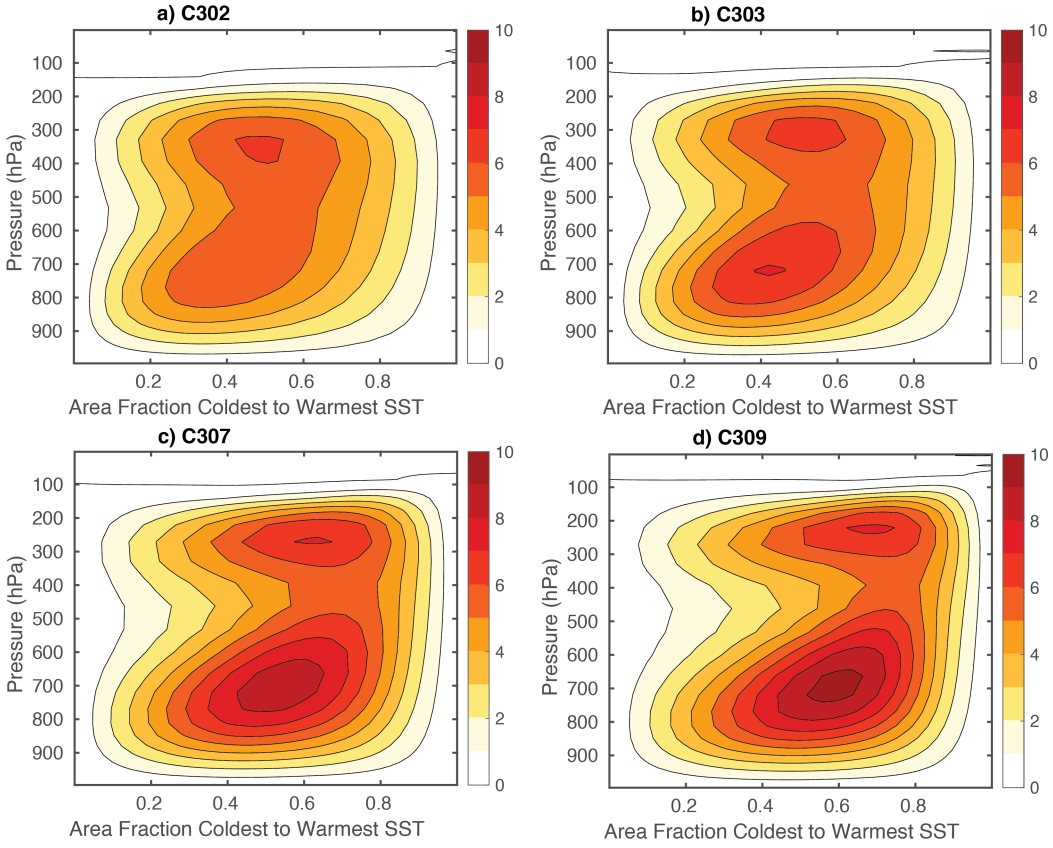

Figure 8. Streamfunction as in Figure 6 for cases a) C302, b) C303, c) C307 and d) C309. Units are kgs^{-1} and contour interval is $1x10^{11}kgs^{-1}$.

Nigam (1997) showed that radiative cooling from stratocumulus tops could drive important shallow circulations. Zhang et al. (2004) gave evidence for the existence of such shallow circulations from reanalysis products. Nolan et al. (2007) suggested that these circulations were analogous to sea breezes driven by SST gradients. Nishant et al. (2016) used regional simulations to argue that radiative driving was a more consistent explanation for the existence of these shallow circulations. Schulz & Stevens (2018) used compositing in moisture space to show that moisture gradients lead to radiative heating anomalies that drive shallow circulations. Convective heating profiles estimated from active remote sensing indicate seasons and locations where the tropical convective heating profile has two maxima in the vertical (Huaman & Takahashi, 2016; Huaman & Schumacher, 2018), as indicated for AM2.1 in Figure 7b . Our model results support the idea that radiative cooling in the subsiding region drives a shallow circulation in the tropics. In addition, we show the important role of radiative cooling from the relative humidity gradient above the boundary layer in deepening that shallow circulation, so that it is not only the moist boundary layer and the clouds within it that are important.

The change in the structure of the streamfunction with mean SST is shown in Figure 8. As the SST increases, the upper cell moves to lower pressure, keeping the temperature at the center of the cell nearly constant, while the lower cell remains attached to the surface. It is interesting that both cells increase in strength as the mean SST is increased. The general consensus is that overturning rates should decrease in a warmed climate because the dry static stability increases, so that the radiative cooling can be

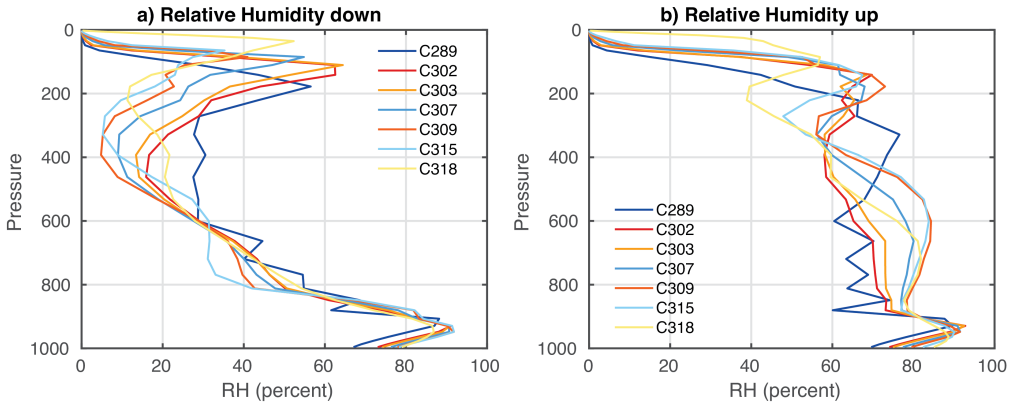

Figure 9. Relative humidity in the a) downward and b) upward regions as functions of air pressure for the seven basic experiments.

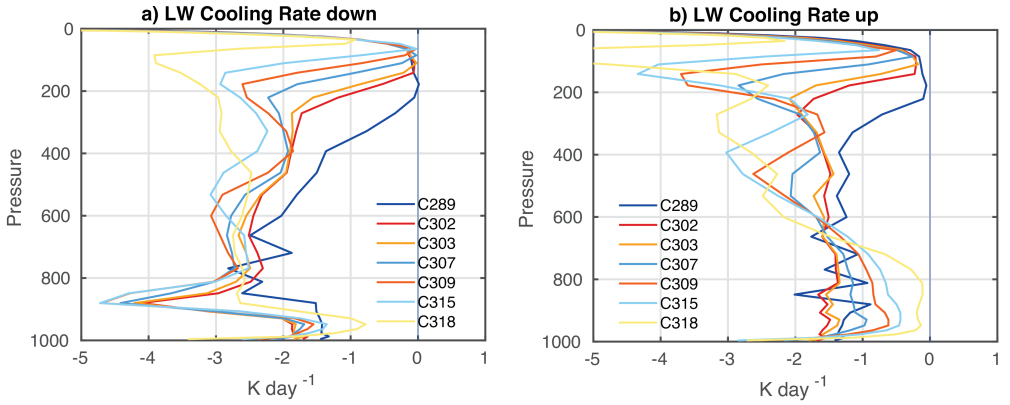

Figure 10. Longwave radiative cooling rate in the a) downward and b) upward regions for the seven basic experiments. (the total radiative heating rate shows similar structural changes)

balanced by a weaker subsidence rate (Knutson & Manabe, 1995; Held & Soden, 2006). In the present simulations the radiative cooling rate increases in magnitude with warming, the subsiding fraction increases slightly and the upward velocity in the region of rising motion increases, so that the mass circulation speeds up with warming, despite the fact that the mean downward vertical velocity in the subsiding region decreases a little with warming. The increasing difference of SST between the rising and subsiding region likely also contributes to the increased mass circulation. Among other effects, increased SST contrast in the tropics results in the atmosphere warming faster than the mean SST, which accelerates atmospheric radiative cooling.

6 Vertical Structure of Humidity and Heating Rate

We next show that the vertical distribution of relative humidity in the upward and downward regions changes modestly with warming SST, and we show that the mass-integrated atmospheric cooling rate increases by extending upward, rather than by increasing at each pressure level. Figure 9 shows the relative humidity in the downward and upward regions for the basic set of experiments. It was previously shown in Figure 1 that the relative humidity in the model is in qualitative agreement with ERA-Interim data for the tropics.

Fig. 10 shows the atmospheric longwave cooling rate as a function of pressure for the seven basic experiments. This plot includes cloud effects, but is not greatly different from the clear-sky plot. In both the downward and upward regions, the mass-integrated cooling rate, which is related to the OLR (Equation 3), increases by extending upward more than by increasing uniformly. In fact, in the lowest troposphere the cooling rate generally weakens with increasing SST. This is especially true in the upward region, where the cooling rate in the lower troposphere weakens with increasing SST below 700hPa. For the warmest cases the longwave cooling rate in the lower troposphere becomes quite small as the atmospheric column approaches a decoupled state that would lead to a runaway greenhouse effect if the whole troposphere was as moist as the upward region (Renno, Emanuel, & Stone, 1994; Renno, Stone, & Emanuel, 1994). The importance of the dry, subsiding region for stabilizing the climate was described by Pierrehumbert (1995).

6.1 1-D RCE Experiments

The upward extension and increase of the cooling rate are a consequence of the nearly moist adiabatic lapse rate and the dependence of water vapor saturation on temperature. This can be demonstrated with a simple one-dimensional radiative-convective equilibrium model. We follow the same adjustment procedure as Manabe & Wetherald (1967), except that the lapse rate relaxes to a moist adiabatic lapse rate with a one-hour time scale. The radiation code is RRTMG (Mlawer et al., 1997; Clough et al., 2005). The model experiments here and interpretation of some convection-resolving experiments by Romps (2014), suggest that the upper-tropospheric relative humidity is nearly a fixed function of temperature. To approximately fit the observed mean profile of relative humidity we use a piecewise linear function of pressure, which is a constant 80% below 850 hPa, declines linearly to a minimum of 40% at the pressure where the temperature is 270K, then increase to 70% where the radiative cooling rate falls to -0.2 $Kday^{-1}$, then declines linearly to a stratospheric value at a pressure that is half of the value where the upper relative humidity peak occurs. This distribution is a reasonable fit to the relative humidity distribution shown in Figure 1b. To be consistent with the GCM and ERA Interim reanalysis, we assume that the saturation vapor pressure transitions linearly from that of liquid at 273K to ice at 253K. As the climate is warmed, the mid-tropospheric minimum and the upper tropospheric maximum in relative humidity tend to maintain a constant temperature as they move to lower pressures. The tendency of the required convective heating rate profile to become more top heavy with increasing surface temperature can be illustrated well enough with a model that has uniform relative humidity, but we will show results for this more realistic profile.

The CO_2 is set to 300ppm, other trace gases are present in their current abundances and the surface albedo is set to 10%. The temperature is varied by changing the insolation as in our GCM experiments, but to get SST values in the range desired, different insolations need to be used depending on the relative humidity profile and whether ozone is included or not.

Figure 11 shows the humidity profiles from the solution to the 1-D RCE computations with climatological tropical ozone fixed as a function of pressure. The pressure of the mid-tropospheric minimum follows a fixed temperature of 270K, while the upper maximum follows the level where the radiative cooling rate falls below -0.2K/day, which also occurs at a nearly fixed temperature. The results are not very sensitive to this choice of -0.2K/day, but since there is no convective overshoot or Brewer-Dobson circulation to support a transition to radiative warming above the top of the convecting layer in this 1-D model, it is felt that a small negative cooling rate threshold would be more robust for computational purposes than zero radiative cooling rate. The five cases represent different surface temperature values that were induced by changing the insolation.

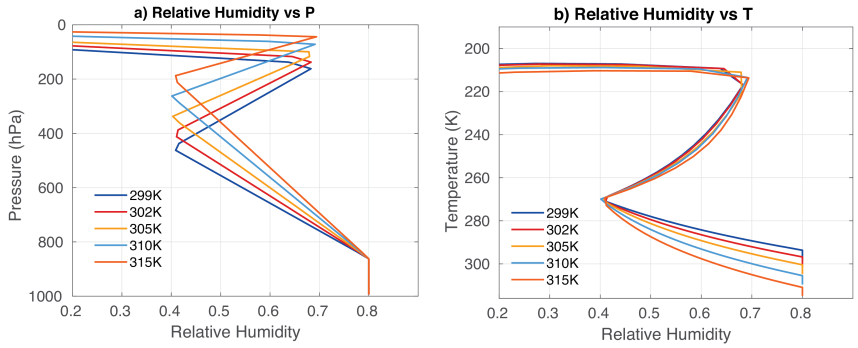

Figure 11. Relative humidity as functions of a) pressure and b) temperature that result from the 1-D RCE calculations shown in Figure 12. Curves are labeled according to the approximate SST.

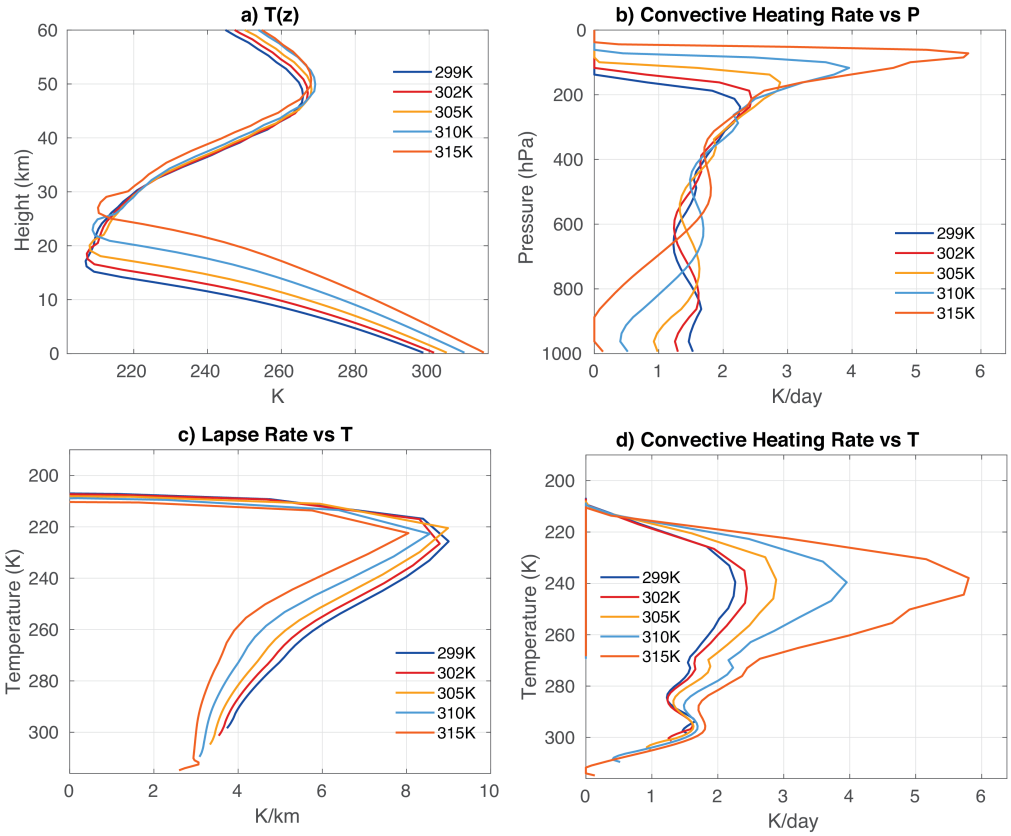

Figure 12. 1-D RCE results for cases with tropical ozone and the relative humidity profiles shown in 11. a) Temperature versus height, b) Convective heating rates as a function of pressure, c) Lapse rate as a function of air temperature and d) Convective heating as a function of air temperature. Note that the convective heating rate is equal to the radiative cooling rate in this 1-D model.

Figure 12 shows the results of RCE computations corresponding to the relative humidity profiles shown in Figure 11. The temperature profile follows a moist adiabat up to about 220K where the lapse rate becomes more stable. This lapse rate kink occurs at very nearly the same air temperature for all SST values, but the maximum lapse rate declines a little with increasing surface temperature as the convecting layer extends into the ozone layer, which is fixed as function of pressure. This is as expected given the dependence of water vapor on temperature alone and the strengths of the rotational emission lines of water vapor (Hartmann & Larson, 2002; Jeevanjee & Fueglistaler, 2020b). The convective heating rate, which is equal to the radiative cooling rate, becomes more top heavy in pressure space (Figure 12b,d). In temperature coordinates the cooling rate profile stays at about the same temperature, but increases in magnitude. Since a 1-D RCE model can produce increasing magnitude but fixed temperature of the cooling rate with increasing SST, we conclude that radiation physics in an environment where the temperature profile approximately follows a moist adiabat is the explanation for this behavior in the GCM and likely also in nature.

The effect of ozone and water vapor on RCE in a cloud-resolving model was studied by Harrop & Hartmann (2012) We also performed 1-D simulations without ozone (see Supplemenary Materials). In the absence of ozone, the lapse rate approaches the dry adiabatic at about 200K, irrespective of surface temperature. The minimum dry stability shows no pressure dependence, and always approaches the dry adiabatic value at the top of the convecting layer. Below that the stability throughout the troposphere is increased because of the assumption of a moist adiabatic temperature profile. While the dry adiabatic lapse rate is independent of pressure, the moist adiabatic lapse rate depends on pressure through the dependence of saturation specific humidity on pressure at a fixed temperature.

6.2 Theoretical Explanation for the Top-heavy Radiative Cooling Profile

The increase in magnitude of the radiative cooling rate with surface temperature can be understood theoretically by using the cooling to space approximation (Rodgers & Walshaw, 1966; Petty, 2006; Jeevanjee & Fueglistaler, 2020a). Begin with the cooling-to-space approximation for the water vapor radiative heating rate at a particular wavelength, λ.

$$\frac{dT}{dt}\Big)_\lambda = -\frac{\pi\, k_\lambda\, \rho_{H_2O}}{\rho_{Air}\, c_p\, \bar{\mu}}\, B_\lambda(T)\, e^{\frac{-\tau_\lambda}{\bar{\mu}}} \tag{9}$$

Here $\bar{\mu} = 1.66^{-1}$ is the average over a hemisphere of $\mu = cos\theta$, $k_\lambda$is the mass absorption coefficient and τ_λ is the normal optical depth from the given height to the top of the atmosphere. Next use the following identity

$$\frac{\rho_{H_2O}}{\rho_{Air}} = 0.622\, RH\, \frac{e_s}{p}. \tag{10}$$

Here RH represents relative humidity and e_s is the saturation vapor pressure. Following the work of Chou et al. (1993) we assume a linear dependence of the mass absorption coefficient on pressure.

$$k_\lambda = k_{\lambda 0}\frac{p}{p_0} \tag{11}$$

So we find that,

$$\frac{dT}{dt}\Big)_\lambda = -\frac{0.622\,\pi}{c_p\, p_0\, \bar{\mu}}\, e_s(T)\, RH\, k_{\lambda 0}\, B_\lambda(T)\, e^{\frac{-\tau_\lambda}{\bar{\mu}}}. \tag{12}$$

We write the optical depth using the hydrostatic approximation as,

$$\begin{aligned}\tau_\lambda &= \int_z^\infty k_\lambda\, \rho_{H_2O}\, dz = \int_0^p k_{\lambda 0}\, \frac{p}{p_0}\, 0.622\, \frac{e_s}{p}\, RH\, \rho_{Air}\, \frac{dp}{g\, \rho_{Air}} \\ &= \frac{k_{\lambda 0}\, 0.622}{g\, p_0} \int_0^p RH\, e_s(T)\, dp = \frac{k_{\lambda 0}\, 0.622}{g\, p_0}\, \overline{RH\, e_s(T)}\, p\end{aligned} \tag{13}$$

So the form we desire is,

$$\frac{dT}{dt}\Big)_\lambda = -\frac{0.622\, \pi}{c_p\, p_0\, \bar{\mu}}\, e_s(T)\, RH\, k_{\lambda 0}\, B_\lambda(T)\, e^{(-C\, k_{\lambda 0}\, \overline{RH\, e_s(T)}\, p)}. \tag{14}$$

Where C is a constant.

$$C = \frac{0.622}{p_0\, g\, \bar{\mu}} \tag{15}$$

In equation (14) he first part represents the emission and the exponential term represents the transmission of this emission. The only pressure dependence is in the optical depth within the exponential representing the transmission, and the emission depends only on temperature. We thus predict that the emission temperature will remain the same, while the cooling rate will increase with warming as the transmission to space becomes more efficient at lower pressures. If we assume, following the Fixed Anvil Temperature (FAT) theory (Hartmann & Larson, 2002) that the cloud emission temperature is approximately fixed independent of surface temperature, then the cooling from clouds will also increase as they move upward in a warmer climate. In the control experiments, the level where the cooling rate peaks moves from 200hPa to 100hPa as the climate warms so the exponent in the transmission term in equation (14) varies by a factor of 2. Thus we believe that we have a good theoretical understanding of the reasons why the cooling rate peaks at a constant temperature, but that peak increases in magnitude as the surface warms.

6.3 Implications of Radiative Cooling for Cloud Ice

Figure 13 shows the convective heating rate and the ice water content as functions of temperature for the control simulations. Both increase in the region where the radiative cooling rate is increasing with SST. It is reasonable to speculate then that the more top-heavy cooling rate profile will lead to enhanced cloud ice. This theory for more cloud ice in a warmed climate has the advantage of being relatively insensitive to assumptions about cloud entrainment and detrainment. An alternative argument might be that in a warmed climate more water is entering the cloud at its base, which is warming, and assuming a fixed precipitation efficiency, one should then expect more cloud mass to result. This enhanced convective heating would be unlikely to continue unless radiative cooling can get rid of the added convective heating, so we propose that the enhanced radiative cooling is necessary and more predictive than assumptions about mass flux and detrainment. Oceanic convection is often close to equilibrated and rather gentle, so it is unclear that more vigorous updrafts would supply more ice to the atmosphere in a warmed climate without the requirement to balance greater radiative cooling rates.

An important consequence of the radiative cooling rate and convective heating rate becoming more top-heavy with increasing SST is that the GCM's parameterizations have to be able to adjust to provide this different heating structure as the climate warms. This is achieved in the GCM used here by increasing the amount of precipitation that is produced by the large-scale scheme as opposed to the convection scheme. The large-scale precipitation is sometimes also referred to as stratiform precipitation. Held et al. (2007) have noted how the GFDL AM2.1 model we are using here produces more grid-scale convection via the large-scale scheme as the SST warms. Figure 14 shows the vertical structure of the convective and large-scale heating rates as functions of air temperature. The

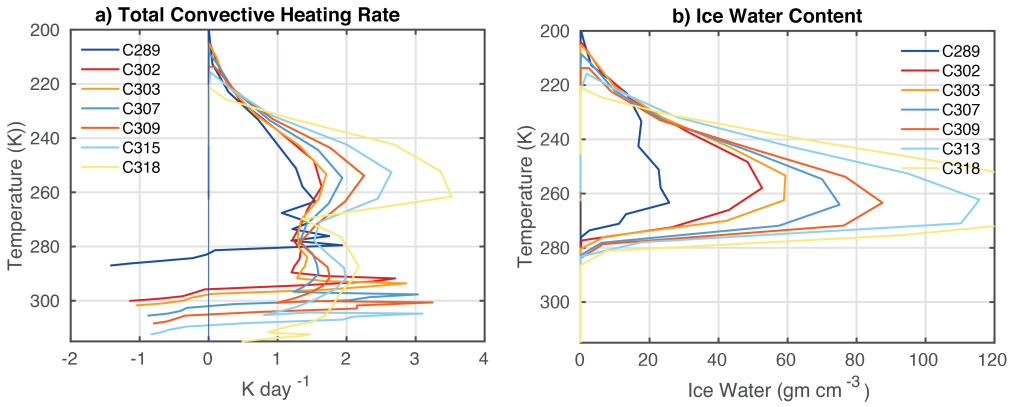

Figure 13. a) Globally averaged total convective heating rate and b) ice concentration as functions of air temperature for the control experiments with AM2.1.

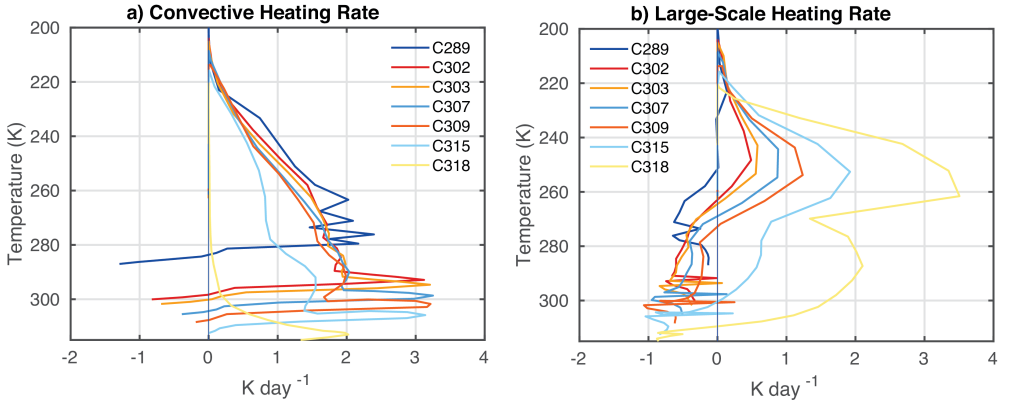

Figure 14. Convective heating rate plotted versus air temperature for the a) convection parameterization and the large-scale parametization for the control experiments with AM2.1.

increase in convective heating rate in the upper troposphere peaking around temperatures of 250K is contributed almost entirely by the large-scale scheme. The convective scheme seems only able to produce a convective heating rate that declines upward. The increasing importance of the large-scale scheme can thus be regarded as the model's response to the requirement that the convective heating balance an increasingly top-heavy radiative cooling profile. One can also see that for the warmest temperatures the convection scheme contributes less as the atmosphere approaches its runaway greenhouse condition. The double maximum in the convective heating rate at warmer temperatures is a signature of the upper circulation cell separating from the lower circulations cell (Figure 13a).

6.4 Low Cloud Response

We next turn to the very modest changes in cloud reflectivity in the region of subsiding velocity. Why does the SWCRE seem to decline a little over the subsiding region with increasing temperature as the SST warms from present values and the SST contrast also increases? Figures 5c,d indicate that the estimated inversion strength (EIS, Wood & Bretherton (2006)) and lower tropospheric stability (LTS, Klein & Hartmann (1993)) both increase in the subsiding region as the climate is warmed above present val-

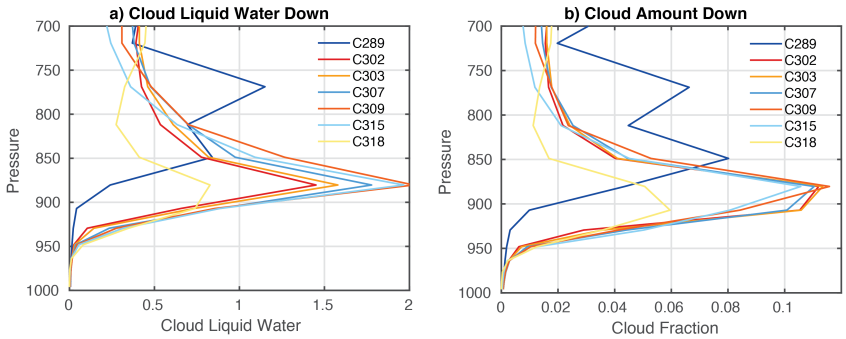

Figure 15. a) Cloud liquid water content (LWC in) and b) cloud fraction below 700hPa in the region of subsiding velocity.

ues. The dynamic forcing associated with enhanced stability would be expected to increase the low cloud fraction and albedo. Figure 15 shows that the cloud fraction stays about constant, and liquid water content increases only slightly in the boundary layer of the subsiding region between C302 and C309, but then declines for the warmest cases C313 and C318. The cloud fraction is approximately constant, until it decreases for SST greater than 310K. The low clouds thus thicken slightly between 302K and 309K mean SST and this would increase the reflectivity of the low clouds. The effect of this increased cloud albedo is offset by the increased absorption of solar radiation in the atmosphere by water vapor as the SST and specific humidity increase. The insolation is also increasing, but the effect of this is minor compared to the large increases in water vapor abundance with temperature.

All else being equal one would expect the dynamical effect of the increased inversion strength to increase the low cloud fraction and albedo in the subsiding region (Klein & Hartmann, 1993; Wood & Bretherton, 2006; Bretherton, 2015)). As the climate warms, however, the vertical gradient of specific humidity in the lower troposphere increases very rapidly with SST. This would be expected to decrease the cloud amount through a thermodynamic mechanism discussed by Bretherton & Blossey (2014) that is related to the increased vertical gradient of moisture in warmed climates (Brient & Bony, 2013). It appears that the dynamic and thermodynamic mechanisms approximately cancel each other in this model, such that the net change in the low cloud radiative effect in the subsiding region is small across a large range of SST. Sherwood et al. (2014) show that the low cloud feedback varies a lot across models in large measure because of differences in the way the thermodynamic effect of increased specific humidity gradients on low clouds is modeled. Other models show a much stronger role for low cloud feedbacks in RCE simulations with slab oceans (Drotos et al., 2020). The rather weak response of low clouds to global warming in this model is consistent with some observational studies that suggest the reflection of solar radiation by low clouds declines with temperature (McCoy et al., 2017; Qu et al., 2015) and that dynamic and thermodynamic effects may strongly offset each other, as they appear to do in these simulations (Myers & Norris, 2016).

7 Conclusion

We have investigated the processes that determine the mean sea surface temperature contrast in a climate model run in Tropical World mode, with no rotation, uniform insolation and a slab ocean model. The mean SST difference between regions of rising and subsiding velocity increases as the climate is warmed above mean SST values comparable to today's. This increase in SST contrast occurs because the clear-sky

greenhouse effect increases more rapidly for the moist atmosphere overlying the region of upward motion and high SST values than for the drier subsiding region with cooler SSTs. Cloud radiative effects generally act to reduce the SST contast as the model is warmed.

The strength of the mass overturning circulation between the warm and the cold SST regions is split into a lower cell and an upper cell. The lower cell is associated with radiative cooling from the humidity decline at and above the boundary layer, especially in the subsiding region where the relative humidity is low. This cell remains at a fixed pressure as the climate warms. The upper cell is associated with radiative cooling near the top of the layer of rapid radiative cooling. It moves upward to lower pressures so as to maintain a relatively constant air temperature as the SST is warmed. The strengths of both circulation cells increase with warming up to a mean SST of 310K, despite the increasing dry static stability associated with the moist adiabatic lapse rate. This is possible because the area of subsiding motion increases and the radiative cooling rate increases as the SST is warmed.

In the particular model used here the global mean albedo does not change much with SST. The albedo decreases slightly with mean SST in the subsiding region where low clouds are present and increases steadily in the region of upward motion and deep convection. The low-cloud albedo in the subsiding region does not change much with SST. We speculate that this is because increases in estimated inversion strength, which should increase low cloud albedo, are offset by thermodynamic processes, which provide more drying of the boundary layer by entrainment of air from above as the SST is increased.

High clouds in the region of upward motion and deep convection become more reflective and increase their ice content with warming. We argue that this occurs because the strength of radiative cooling in the air temperature regime where ice clouds form is strengthened with warming. As the SST is warmed the radiative cooling rate of the atmosphere strengthens by extending higher and increasing in magnitude, while the cooling rate in the lower troposphere remains approximately constant or declines. This can be understood as a purely clear-sky radiative effect by considering a one-dimensional radiative-convective equilibrium model, and using the cooling to space approximation. One can then conclude that the amount of ice in the tropical atmosphere should increase with warming, if the ice amount is proportional to the radiative cooling rate in the atmospheric layers where ice is formed. The increasingly top-heavy structure of the radiative cooling profile may be a partial explanation for why the precipitation in the model shifts progressively from the convection parameterization to the large-scale parameterization as the climate warms. The convection parameterization produces a bottom-heavy convective heating profile at all SST values.

Below 310K the efficient cooling from the region of subsiding motion keeps the TW climate relatively insensitive, warming only about 0.26K for each Wm^{-2} of forcing. In the region of subsiding motion, the greenhouse effect feedback is nearly absent and the OLR increases at almost the rate that would be predicted from the Planck emission of the surface temperature. As the mean SST approaches 310K and the temperature in the region of rising motion approaches 315K, the SST difference begins to decline with warming and the climate of the model becomes more sensitive to further positive climate forcing.

Very strong positive feedbacks are engaged as the SST contrast begins to decline, which both lead to further decreases of the SST contrast and a more unstable global climate. Much of the reason for this sudden change appears to originate in the increasing amount of water vapor in the lower atmosphere. In the subsiding region the OLR begins to increase more slowly with SST above 310K, because the emission from the atmosphere becomes less sensitive to SST, while the contribution from surface emission also declines. In the region of rising motion, the contribution of surface emission to OLR

reaches a limiting minimum value, while the emission from the atmosphere continues to increase approximately linearly with SST, so that the sensitivity of OLR to SST increases above 310K. As the SST contrast declines in response to changes in the longwave radiative feedbacks in the rising and subsiding regions, the reduction in SST contrast also drives a decline in the reflectivity of the low clouds in the subsiding region and an increase in the reflectivity of the clouds in the rising region. An increase in climate sensitivity at high temperatures is driven mostly by the decreased efficiency of the emission from the subsiding region to cool the system, but reductions in cloud clouds with SST also contribute.

The elevation and strengthening of the radiative cooling profile while remaining at a relatively constant temperature is very likely a robust effect that is independent of any approximations in the model. It is shown to follow from the basic physics of clear-sky radiative transfer, and it is very likely to carry over to cloudy skies, since we expect the high clouds to also remain at a relatively constant temperature and transmit through a thinner atmosphere as the climate warms.

The separation of the overturning circulation into a shallow cell driven by shallow radiative cooling and a deeper cell driven by deep radiative cooling also seems to be a potentially robust result, which should be further studied in observations and in global warming simulations with more realistic configurations. It also seems quite reasonable to expect the lower cell to remain attached to the surface while the upper cell extends upward following the radiative cooling rate and thereby maintain a roughly constant temperature as it does so. The increased overturning rate of the shallow cell associated with the increased radiative cooling rates that are associated with the humidity gradients in the subsiding region is also worthy of further study.

Other features of these simulations are more sensitive to the parameterizations. The increase in cloud ice in the model, although a consistent result of the elevated heating profile, is very sensitive the to parameterizations used to relate convective heating to net ice production. The relationship of radiative cooling rate to cloud ice amount is probably best undertaken with a model in which deep convection is explicitly resolved and coupled to realistic cloud microphysics. The low clouds in the model are parameterized and low cloud response to warming is known to be a major cause of uncertainty in global warming simulations. The low clouds in our simulations respond very little to global warming. It is possible that in another model the low clouds could respond strongly to warming and be an important driver of changed SST constrast. Finally, of course, rotation, realistic continental geography, and ocean heat transports likely greatly modify the responses seen in TW simulations, and may alter the relative importance of water vapor, cloud and circulation feedbacks on climate change.

Acknowledgments

This work was supported by the National Science Foundation under Grant AGS-1549579. QF is partially supported by NSF AGS-1821437. PB was supported in part by NSF grant OISE-1743753. Blaž Gasparini and Stephen A. Klein provided useful comments. The paper was improved by critical comments from reviewers. We are grateful to GFDL-NOAA for providing the GCM model code used here and for the data providers cited. Model data supporting the figures and associated software can be found here

http://hdl.handle.net/1773/46293

References

Albern, N., Voigt, A., Buehler, S. A., & Grutzun, V. (2018). Robust and nonrobust impacts of atmospheric cloud-radiative interactions on the tropical circulation and its response to surface warming. *Geophys. Res. Lett.*, *45*(16), 8577-8585. doi:

10.1029/2018gl079599

Anderson, J. L., Balaji, V., Broccoli, A. J., Cooke, W. F., Delworth, T. L., Dixon, K. W., ... Dev, G. G. A. M. (2004). The new gfdl global atmosphere and land model am2-lm2: Evaluation with prescribed sst simulations. *J. Climate*, *17*(24), 4641-4673.

Andrews, T., Gregory, J. M., Paynter, D., Silvers, L. G., Zhou, C., Mauritsen, T., ... Titchner, H. (2018). Accounting for changing temperature patterns increases historical estimates of climate sensitivity. *Geophys. Res. Lett.*, *45*(16), 8490-8499. doi: 10.1029/2018gl078887

Becker, T., Stevens, B., & Hohenegger, C. (2017). Imprint of the convective parameterization and sea-surface temperature on large-scale convective self-aggregation. *J. Adv. Model. Earth Sys.*, *9*(2), 1488-1505. doi: 10.1002/2016ms000865

Birner, T. (2010). Residual circulation and tropopause structure. *Journal of the Atmospheric Sciences*, *67*(8), 2582-2600. doi: 10.1175/2010jas3287.1

Bony, S., Stevens, B., Coppin, D., Becker, T., Reed, K., Voigt, A., & Medeiros, B. (2016). Thermodynamic control of anvil-cloud amount. *Proc. Nat. Acad. Sci. U. S. A.*, *113*(32), 8927-8932. doi: doi:10.1073/pnas.1601472113

Bretherton, C. S. (2015). Insights into low-latitude cloud feedbacks from high-resolution models. *Phil. Trans. Roy. Soc. A*, *373*(2054). doi: 10.1098/rsta.2014.0415

Bretherton, C. S., & Blossey, P. N. (2014). Low cloud reduction in a greenhouse-warmed climate: Results from lagrangian les of a subtropical marine cloudiness transition. *Journal of Advances in Modeling Earth Systems*, *6*(1), 91-114. doi: 10.1002/2013ms000250

Bretherton, C. S., Blossey, P. N., & Khairoutdinov, M. (2005). An energy-balance analysis of deep convective self-aggregation above uniform sst. *J. Atmos. Sci.*, *62*(12), 4273-4292.

Brient, F., & Bony, S. (2013). Interpretation of the positive low-cloud feedback predicted by a climate model under global warming. *Climate Dynamics*, *40*(9-10), 2415-2431. doi: 10.1007/s00382-011-1279-7

Chou, M. D., Ridgway, W. L., & Yan, M. M. H. (1993). One-parameter scaling and exponential-sum fitting for water vapor and co/sub 2/ infrared transmission functions. *J. Atmos. Sci.*, *50*(14), 2294-2303.

Clement, A. C., Seager, R., Cane, M. A., & Zebiak, S. E. (1996). An ocean dynamical thermostat. *J. Climate*, *9*(9), 2190-2196.

Clough, S. A., Shephard, M. W., Mlawer, E., Delamere, J. S., Iacono, M., Cady-Pereira, K., ... Brown, P. D. (2005). Atmospheric radiative transfer modeling: a summary of the aer codes. *J. Quanti. Spectros. Rad. Trans.*, *91*(2), 233-244. doi: 10.1016/j.jqsrt.2004.05.058

Coppin, D., & Bony, S. (2015). Physical mechanisms controlling the initiation of convective self-aggregation in a general circulation model. *J. Adv. Model. Earth Systems*, *7*(4), 2060-2078. doi: 10.1002/2015ms000571

Coppin, D., & Bony, S. (2017). Internal variability in a coupled general circulation model in radiative-convective equilibrium. *Geophys. Res. Lett.*, *44*(10), 5142-5149. doi: 10.1002/2017gl073658

Cronin, T. W., & Wing, A. A. (2017). Clouds, circulation, and climate sensitivity in a radiative-convective equilibrium channel model. *J. Adv. Model. Earth Sys.*, *9*(8), 2883-2905. doi: 10.1002/2017ms001111

Dee, D. P., Uppala, S. M., Simmons, A. J., Berrisford, P., Poli, P., Kobayashi, S., ... Vitart, F. (2011). The era-interim reanalysis: configuration and performance of the data assimilation system. *Quart. J. Royal Met. Soc.*, *137*(656), 553-597. doi: 10.1002/qj.828

Delworth, T. L., Broccoli, A. J., Rosati, A., Stouffer, R. J., Balaji, V., Beesley, J. A., ... Zhang, R. (2006). Gfdl's cm2 global coupled climate models. part i:

779 Formulation and simulation characteristics. *J. Climate*, *19*(5), 643-674. doi:
780 10.1175/jcli3629.1
781 Dong, Y., Proistosescu, C., Armour, K. C., & Battisti, D. S. (2019, June). Attribut-
782 ing Historical and Future Evolution of Radiative Feedbacks to Regional Warming
783 Patterns using a Green's Function Approach: The Preeminence of the Western
784 Pacific. *Journal of Climate*, *32*(17), 5471–5491. doi: 10.1175/JCLI-D-18-0843.1
785 Drotos, G., Becker, T., Mauritsen, T., & Stevens, B. (2020). Global vari-
786 ability in radiative-convective equilibrium with a slab ocean under a wide
787 range of co2 concentrations [Journal Article]. *Tellus A*, *72*(1), 1-19. doi:
788 10.1080/16000870.2019.1699387
789 Harrop, B. E., & Hartmann, D. L. (2012). Testing the role of radiation in determin-
790 ing tropical cloud-top temperature. *J.Climate*, *25*(17), 5731-5747. doi: 10.1175/
791 jcli-d-11-00445.1
792 Harrop, B. E., & Hartmann, D. L. (2015). The relationship between atmospheric
793 convective radiative effect and net energy transport in the tropical warm pool.
794 *Journal of Climate*, *28*(21), 8620-8633. doi: 10.1175/jcli-d-15-0151.1
795 Harrop, B. E., & Hartmann, D. L. (2016). The role of cloud radiative heating in
796 determining the location of the itcz in aquaplanet simulations. *J. Climate*, *29*(8),
797 2741-2763. doi: 10.1175/jcli-d-15-0521.1
798 Hartmann, D. L. (2016). *Global physical climatology* (2nd ed.) [Book]. Elsevier.
799 Hartmann, D. L., Blossey, P., & Dygert, B. (2019). Convection and climate: What
800 have we learned from simple models and simplified settings? *Curr. Clim. Change*
801 *Rep.*, *5*(3), 196-206. doi: 10.1007/s40641-019-00136-9
802 Hartmann, D. L., & Larson, K. (2002). An important constraint on trop-
803 ical cloud-climate feedback. *Geophys. Res Lett.*, *29*(20), 1951-1954. doi:
804 doi:10.1029/2002GL015835
805 Held, I. M., Hemler, R. S., & Ramaswamy, V. (1993). Radiative-convective equilib-
806 rium with explicit two-dimensional moist convection. *J. Atmos. Sci.*, *50*(23), 3909-
807 3927.
808 Held, I. M., & Soden, B. J. (2006). Robust responses of the hydrological cycle to
809 global warming. *J. Climate*, *19*(21), 5686-5699.
810 Held, I. M., Zhao, M., & Wyman, B. (2007). Dynamic radiative-convective equilibria
811 using gcm column physics. *J. Atmos. Sci.*, *64*(1), 228-238.
812 Huaman, L., & Schumacher, C. (2018). Assessing the vertical latent heating struc-
813 ture of the east pacific itcz using the cloudsat cpr and trmm pr. *Journal of Cli-*
814 *mate*, *31*(7), 2563-2577. doi: 10.1175/jcli-d-17-0590.1
815 Huaman, L., & Takahashi, K. (2016). The vertical structure of the eastern pacific
816 itczs and associated circulation using the trmm precipitation radar and in situ
817 data. *Geophys. Res. Lett.*, *43*(15), 8230-8239. doi: 10.1002/2016gl068835
818 Inamdar, A. K., & Ramanathan, V. (1994). Physics of greenhouse effect and convec-
819 tion in warm oceans. *J. Climate*, *7*(5), 715-31.
820 Jeevanjee, N., & Fueglistaler, S. (2020a). On the cooling-to-space approximation. *J.*
821 *Atmos. Sci.*, *77*(2), 465-478. doi: 10.1175/jas-d-18-0352.1
822 Jeevanjee, N., & Fueglistaler, S. (2020b). Simple spectral models for atmospheric ra-
823 diative cooling. *J. Atmos. Sci.*, *77*(2), 479-497. doi: 10.1175/jas-d-18-0347.1
824 Klein, S., & Hartmann, D. (1993). The seasonal cycle of low stratiform clouds. *J.*
825 *Climate*, *6*(8), 1587-1606.
826 Knutson, T. R., & Manabe, S. (1995). Time-mean response over the tropical pa-
827 cific to increased co2 in a coupled ocean-atmosphere model. *J. Climate*, *8*(9),
828 2181-2199.
829 Kohyama, T., Hartmann, D. L., & Battisti, D. S. (2017). La nina-like mean-state
830 response to global warming and potential oceanic roles. *J. Climate*, *30*(11), 4207-
831 4225. doi: 10.1175/jcli-d-16-0441.1
832 Koll, D. D. B., & Cronin, T. W. (2018). Earth's outgoing longwave radiation lin-

ear due to h2o greenhouse effect [Journal Article]. *Proc. Nat. Acad. Sci. U. S. A.*, *115*(41), 10293-10298. doi: 10.1073/pnas.1809868115

Larson, K., & Hartmann, D. L. (2003a). Interactions among cloud, water vapor, radiation, and large-scale circulation in the tropical climate. part ii: Sensitivity to spatial gradients of sea surface temperature. *J. Climate*, *16*(10), 1441-1455.

Larson, K., & Hartmann, D. L. (2003b). Interactions among cloud, water vapor, radiation, and large-scale circulation in the tropical climate. part i: Sensitivity to uniform sea surface temperature changes. *J. Climate*, *16*(10), 1425-1440.

Loeb, N., Doelling, D. R., Wang, H., Su, W., Nguyen, C., Corbett, J., ... Kato, S. (2018). Clouds and the earth's radiant energy system (ceres) energy balanced and filled (ebaf) top-of-atmosphere (toa) edition-4.0 data product. *J. Climate*, *31*(15 January 2018), 895-918. doi: doi.org/10.1175/JCLI-D-17-0208.1

Manabe, S., & Wetherald, R. (1967). Thermal equilibrium of the atmosphere with a given distribution of relative humidity. *J. Atmos. Sci.*, *24*, 241-259.

McCoy, D. T., Eastman, R., Hartmann, D. L., & Wood, R. (2017). The change in low cloud cover in a warmed climate inferred from airs, modis, and era-interim. *J. Climate*, *30*(10), 3609-3620. doi: 10.1175/jcli-d-15-0734.1

Meraner, K., Mauritsen, T., & Voigt, A. (2013). Robust increase in equilibrium climate sensitivity under global warming [Journal Article]. *Geophys. Res. Lett.*, *40*(22), 5944-5948. doi: 10.1002/2013gl058118

Miller, R. (1997). Tropical thermostats and low cloud cover. *J. Climate*, *10*(3), 409-440.

Mlawer, E. J., Taubman, S. J., Brown, P. D., Iacono, M. J., & Clough, S. A. (1997). Radiative transfer for inhomogeneous atmospheres: Rrtm, a validated correlated-k model for the longwave. *J Geophys. Res.-Atmos.*, *102*(D14), 16663-16682. doi: 10.1029/97JD00237

Myers, T. A., & Norris, J. R. (2016). Reducing the uncertainty in subtropical cloud feedback. *Geophys. Res. Lett.*, *43*(5), 2144-2148. doi: 10.1002/2015gl067416

Nigam, S. (1997). The annual warm to cold phase transition in the eastern equatorial pacific: diagnosis of the role of stratus cloud-top cooling. *J. Climate*, *10*(10), 2447-67.

Nishant, N., Sherwood, S. C., & Geoffroy, O. (2016). Radiative driving of shallow return flows from the itcz. *J. Adv. Model. Earth Sys.*, *8*(2), 831-842. doi: 10.1002/2015ms000606

Nolan, D. S., Zhang, C., & Chen, S. H. (2007). Dynamics of the shallow meridional circulation around intertropical convergence zones. *J. Atmos. Sci.*, *64*(7), 2262-2285. doi: 10.1175/jas3964.1

Pendergrass, A. G., & Hartmann, D. L. (2014). The atmospheric energy constraint on global-mean precipitation change [Journal Article]. *J. Climate*, *27*(2), 757-768. doi: 10.1175/jcli-d-13-00163.1

Petty, G. (2006). *A first course in atmospheric radiation* [Book]. Madison, Wisconsin: Sundog Publising.

Pierrehumbert, R. (1995). Thermostats, radiator fins and the local runaway greenhouse. *J. Atmos. Sci.*, *52*, 1784-1806.

Popke, D., Stevens, B., & Voigt, A. (2013). Climate and climate change in a radiative-convective equilibrium version of echam6. *J. Adv. Model. Earth Sys.*, *5*(1), 1-14. doi: 10.1029/2012ms000191

Qu, X., Hall, A., Klein, S. A., & DeAngelis, A. M. (2015). Positive tropical marine low-cloud cover feedback inferred from cloud-controlling factors. *Geophysical Research Letters*, *42*(18), 7767-7775. doi: 10.1002/2015GL065627

Ramanathan, V., & Collins, W. (1991). Thermodynamic regulation of ocean warming by cirrus clouds deduced from observations of the 1987 el nino. *Nature*, *351*(6321), 27-32.

Reed, K. A., Medeiros, B., Bacmeister, J. T., & Lauritzen, P. H. (2015). Global

radiative-convective equilibrium in the community atmosphere model, version 5. *J. Atmos. Sci.*, *72*(5), 2183-2197. doi: 10.1175/jas-d-14-0268.1

Renno, N. O., Emanuel, K. A., & Stone, P. H. (1994). Radiative-convective model with an explicit hydrologic cycle. 1. formulation and sensitivity to model parameters. *Journal of Geophysical Research*, *99*(D7), 14429-41.

Renno, N. O., Stone, P. H., & Emanuel, K. A. (1994). Radiative-convective model with an explicit hydrologic cycle. 2. sensitivity to large changes in solar forcing. *Journal of Geophysical Research*, *99*(D8), 17001-20.

Retsch, M. H., Mauritsen, T., & Hohenegger, C. (2019). Climate change feedbacks in aquaplanet experiments with explicit and parametrized convection for horizontal resolutions of 2,525 up to 5 km. *J. Adv. Mod. Earth Sys.*, *11*(7), 2070-2088. doi: 10.1029/2019ms001677

Reynolds, R. W., Smith, T. M., Liu, C., Chelton, D. B., Casey, K. S., & Schlax, M. G. (2007). Daily high-resolution-blended analyses for sea surface temperature. *J. Climate*, *20*(22), 5473-5496. doi: 10.1175/2007jcli1824.1

Rodgers, C., & Walshaw, C. (1966). The computation of infrared cooling rate in planetary atmospheres. *Quart. J. Roy. Meteor. Soc.*, *92*, 67-92.

Romps, D. M. (2014). An analytical model for tropical relative humidity. *J. Climate*, *27*(19), 7432-7449. doi: 10.1175/jcli-d-14-00255.1

Russell, G. L., Lacis, A. A., Rind, D. H., Colose, C., & Opstbaum, R. F. (2013). Fast atmosphere-ocean model runs with large changes in co2 [Journal Article]. *Geophys. Res. Lett.*, *40*(21), 5787-5792. doi: 10.1002/2013gl056755

Schulz, H., & Stevens, B. (2018). Observing the tropical atmosphere in moisture space. *J. Atmos. Sci.*, *75*(10), 3313-3330. doi: 10.1175/jas-d-17-0375.1

Seager, R., Cane, M., Henderson, N., Lee, D. E., Abernathey, R., & Zhang, H. H. (2019). Strengthening tropical pacific zonal sea surface temperature gradient consistent with rising greenhouse gases. *Nature Climate Change*, *9*(7), 517-+. doi: 10.1038/s41558-019-0505-x

Sherwood, S. C., Bony, S., & Dufresne, J. L. (2014). Spread in model climate sensitivity traced to atmospheric convective mixing. *Nature*, *505*(7481), 37-+. doi: 10.1038/nature12829

Tompkins, A. M. (2001a). On the relationship between tropical convection and sea surface temperature. *J. Climate*, *14*(5), 633-637. doi: 10.1175/1520-0442(2001)014⟨0633:otrbtc⟩2.0.co;2

Tompkins, A. M. (2001b). Organization of tropical convection in low vertical wind shears: The role of water vapor. *J Atmos. Sci.*, *58*(6), 529-545. doi: 10.1175/1520-0469(2001)058⟨0529:ootcil⟩2.0.co;2

Vecchi, G. A., & Soden, B. J. (2007). Global warming and the weakening of the tropical circulation. *Journal of Climate*, *20*(17), 4316-4340. doi: 10.1175/jcli4258.1

Waliser, D., & Graham, N. (1993). Convective cloud systems and warm-pool sea surface temperatures: coupled interactions and self-regulation. *J. Geophys. Res. Atmos.*, *98*(D7), 12881-93.

Wing, A. A., & Emanuel, K. A. (2014). Physical mechanisms controlling self-aggregation of convection in idealized numerical modeling simulations. *J. Adv. Model. Earth Sys.*, *6*(1), 59-74. doi: 10.1002/2013ms000269

Wing, A. A., Reed, K. A., Satoh, M., Stevens, B., Bony, S., & Ohno, T. (2018). Radiative-convective equilibrium model intercomparison project. *Geosci. Model Dev.*, *11*(2), 793-813. doi: 10.5194/gmd-11-793-2018

Wing, A. A., Stauffer, C., Becker, T., Reed, K., Ahn, M., Arnold, N., ... al., e. (2020). Clouds and convective self-aggregation in a multi-model ensemble of radiative-convective equilibrium simulations. *J. Adv. Mod. Earth Sys.*, submitted.

Wood, R., & Bretherton, C. S. (2006). On the relationship between stratiform low cloud cover and lower-tropospheric stability. *J. Climate*, *19*(24), 6425-6432.

941 Zhang, C. D., McGauley, M., & Bond, N. A. (2004). Shallow meridional circulation
942 in the tropical eastern pacific. *J. Climate*, *17*(1), 133-139.
943 Zhao, M. (2014). An investigation of the connections among convection, clouds, and
944 climate sensitivity in a global climate model. *J. Climate*, *27*(5), 1845-1862. doi:
945 10.1175/jcli-d-13-00145.1
946 Zhao, M., Golaz, J. C., Held, I. M., Ramaswamy, V., Lin, S. J., Ming, Y., ... Guo,
947 H. (2016). Uncertainty in model climate sensitivity traced to representations of
948 cumulus precipitation microphysics [Journal Article]. *J. Climate*, *29*(2), 543-560.
949 doi: 10.1175/jcli-d-15-0191.1
950 Zhou, C., Zelinka, M. D., & Klein, S. A. (2016). Impact of decadal cloud variations
951 on the earth's energy budget. *Nature Geoscience*, *9*(12), 871-+. doi: 10.1038/
952 ngeo2828